Investigation of plasma instabilities in the stagnated Z pinch

V. V. Ivanov, J. P. Chittenden, R. C. Mancini, D. Papp, N. Niasse, S. D. Altemara, and A. A. Anderson

Phys. Rev. E **86**, 046403 — Published 22 October 2012

DOI: 10.1103/PhysRevE.86.046403

Investigation of plasma instabilities in the stagnated Z pinch

V. V. Ivanov[1], J. P. Chittenden[2], R. C. Mancini[1], D. Papp[1], N. Niasse[2], S. D. Altemara[1], A. A. Anderson[1]

[1]*Department of Physics, University of Nevada, Reno, NV 89557, USA*
[2]*Blackett Laboratory, Imperial College, London SW7 2BZ, UK*

High resolution laser probing diagnostics at the wavelength of 266 nm allow observation of the internal structure and instabilities in dense stagnated Z-pinches, typically, hidden by trailing material. The internal structure of the 1 MA Z-pinch includes strong kink and sausage instabilities, loops, flares, and disruptions. Mid- and small-scale density perturbations develop in the precursor and main pinch. The three-dimension shape and dynamics of the wire-array Z pinch is predetermined by the initial configuration of the wire array. Cylindrical, linear, and star wire-array Z pinches present different sets of instabilities seeded to the pinch at the implosion stage. Prolonged implosion of trailing mass can enhance x-ray production in wire arrays. Fast plasma motion with a velocity >100 km/s was observed in the Z pinch at stagnation with two-frame shadowgraphy. Development of instabilities in wire arrays is in agreement with three-dimensional magnetohydrodynamic simulations.

PACS numbers: 52.59.Qy, 52.58.Lq, 52.35.Py

I. Introduction

Z-pinches are the most powerful and efficient laboratory sources of x-ray radiation. Z-pinches have been applied to different areas of high energy density laboratory plasmas including laboratory astrophysics and inertial confinement fusion researches [1-5]. Plasma instabilities play a crucial role in physics of Z pinches. Z pinches are unstable to many kinds of plasma perturbations which limit power and energy of the generated x-ray pulse [6]. Instabilities rise at the ablation stage and are seeded to the pinch during the implosion [6-12]. Mitigation of implosion plasma inhomogeneity in nested cylindrical, star wire arrays and multi-shell gas puffs helps to generate enhanced x-ray power [2, 13]. The stagnated Z-pinch is unstable to both the m=0 and m=1 magnetohydrodynamic (MHD) perturbations. Some methods help to stabilize the m=0 perturbation but Z-pinch is always unstable to m=1 kink instability [14]. The growth of instabilities at the stagnation stage, finally, destroys the pinch. Instabilities generate "bright" ("hot") spots on Z-pinches with the enhanced electron temperature and density [15-18]. "Hot spots" can strongly contribute to the energy balance and neutron yield in Z pinches. Plasma instabilities predetermine a radiative ability and other plasma parameters in the Z pinch. Some of the expected plasma perturbations are in the micron range and need in high spatial resolution plasma diagnostics for investigation. Laser radiation in the optical region is subjected by strong absorption in dense plasma and cannot pass through the stagnated Z-pinch. The structure and plasma dynamics in the stagnated pinch has been studied with x-ray time-gated pinhole cameras crystal imaging diagnostics, and streak cameras [3, 19]. X-ray self-radiation diagnostics derive, mostly, a temperature map of the pinch with spatial resolution of 70-150 μm. X-ray backlighting was applied to X pinches and single wires [20, 21] at currents <0.5 MA and to wire arrays at the ablation and implosion stages [9, 22-24].

Recently, laser diagnostics at the wavelength of 266 nm were applied to the 1 MA Z pinch [25]. The significantly smaller absorption and refraction in dense plasma at 266 nm makes it

possible to study of the internal structure of the dense Z pinches with well established optical diagnostics. This can help to identify mechanisms of "enhanced" plasma heating in the stagnated pinch [26].

In this paper we present a review of plasma instabilities in 1 MA wire-array Z pinches studied with UV and x-ray diagnostics. Different types of wire arrays create different three-dimensional (3D) structures in Z pinches at the stagnation stage. Large diameter cylindrical wire array implode to the pinch with strong m=0, 1 instabilities and low density. Cylindrical arrays with diameters of 8-16 mm seed strong kink instability in the pinch. The "bead-chain" Z-pinch is typical for planar and small-diameter cylindrical wire arrays. Kink instability is less pronounced in star wire array but breaks also rise on the pinch. Mid-scale periodical instability was observed on the pinch edges. Small-scale perturbations were found at the stagnated pinch. Two-frame shadowgraphy shows fast plasma motion at stagnation, formation of breaks, necks, and plasma "bridges" near necks. UV and x-ray images show that the maximum x-ray power is radiated by Z pinches distorted by kink and sausage instabilities. Fast plasma motion was observed in the Z pinch at stagnation. Prolonged implosion and kinetic energy of plasma generated in the unstable Z pinch with strong instabilities may explain the enhance plasma heating in small-diameter wire-array Z pinches. The maximum power of x-ray radiation is generated by the pinch with strong plasma instabilities. Spectroscopic measurements showed that bright spots on the pinch, typical in compact wire arrays, have an enhanced electron temperature. Three-dimensional MHD simulations of the growth of plasma instabilities in wire-array Z pinches from the ablation to stagnation stages are in a good agreement with experiments.

II. Experimental setup

Experiments were carried out on the pulsed power Zebra generator at the University of Nevada, Reno. The Zebra generator produces a 1-MA current pulse with the rising edge of 80 ns from 10% to 90%, and current prepulse of 200 ns [27]. The impedance of the transmission line is 1.9 Ω. The current is measured with a set of B-dot probes. Wire-array loads are installed on the axis of the vacuum chamber in the return current cage 9 cm in diameter. A configuration of the anode-cathode area allows placing of optical elements and other diagnostics closely to the Z pinch in the vacuum chamber of the Zebra generator [28].

Plasma diagnostics includes laser probing, optical diagnostics, x-ray imaging and spectroscopy. The laser probing includes regular diagnostics at the wavelength of 532 nm located in two directions (with 22.5° between directions) and ultraviolet (UV) diagnostics at 266 nm in the third direction [29]. Two 0.2 ns laser pulses at wavelengths of 532 and 266 nm are generated by two Nd:YAG lasers with pulse energies of 50 mJ. Short pulses provide instant images of the Z-pinch on charge-coupled devices (CCD). Radiation from Z-pinch plasma is blocked by the narrowband spectral filters. Laser diagnostics at the wavelength of 532 nm were used in a four-frame shadowgraphy configuration [30]. The UV channel was used as one-frame shadowgraphy and differential interferometry or two-frame shadowgraphy. In the two-frame configuration, two laser pulses were propagated with different delays and orthogonal linear polarization. Polarizers separated two pulses with different polarizations and delays and transmitted to the appropriate CCD cameras. A field of view of the UV diagnostics on the central part of the pinch was of 3.5-5 mm. The first two-component lens of the beampath was installed in the vacuum chamber of the Zebra generator. The angle of acceptance of the first lens was 14°. This provided high spatial resolution of the UV beampath. The spatial resolution limited by the CCD cameras was 2.5-4

μm/pixel depending on the magnification of the beampath. A UV channel with regular magnification, field of view of 8 mm, and resolution of 12 μm was also used in some series of shots. Shadowgrams at 532 nm and 266 nm are complementary and show plasma in different density ranges. All 266 nm and 532 nm laser channels were spatially co-aligned with a removable needle. The needle was placed on the center of the wire-array load for the reference shots and removed before the main shot of the Zebra generator. The intensity of UV laser beam on CCD cameras was increased by the factor of 3-5 during Zebra shots, compared to reference shots, to mitigate absorption in the trailing material. In 1 MA Z-pinches, the trailing mass can have ~30% of the total load mass [8]. A slit was installed in a series of shots before the CCD camera to provide enhanced illumination of the central area of the pinch and block illumination of sides by laser pulse. The intensity of UV light on the slit was increased by a factor of 30-50 during the Zebra shot for mitigation of strong absorption in the dense pinch. The structure of background laser radiation was recorded on the CCD camera during the reference laser shots. In these shots the structure of the dense pinch was investigated.

The x-ray pulse shape and energy was measured with filtered photoconductive (PCD) and x-ray diodes (XRD) diodes and a bared Ni bolometer [18]. The x-ray from PCD filtered with 8 μm Be foil was used for timing with laser and x-ray images. An x-ray six-frame time-gated pinhole camera recorded 6x2 images with a frame duration of 3 ns in spectral ranges $E_1 > 0.8$ keV and $E_2 > 3$ keV. A spatial resolution of the pinhole camera was 0.25 mm in the first series of shot and improved to 0.18 mm at E_2 and 0.07 mm at E_1 in later shots. X-ray spectra were recorded with a time-integrated spatially-resolved spectrometer with a convex KAP crystal and resolution power of 350. X-ray camera was synchronized with laser imaging. The x-ray keV pulse from the PCD filtered by Be 8 μm foil was used for timing of the pinch stage relative to diagnostics. An x-ray spectrometer with a convex KAP crystal and spatial resolution of 0.45 mm was used to derive electron temperature and density. We investigated aluminum (alloys 5056 and 1199), nickel, and tungsten Z-pinches produced by cylindrical, linear and star wire-arrays, 2 cm tall, with masses from 25 to 90 μg/cm. Appropriate orientation of the wire array to the UV laser beam helps to minimize an impact of the non-imploded plasma on imaging the stagnated pinch.

III. Plasma instability in wire-array Z-pinches at stagnation

UV laser probing demonstrates a significant advantage compared to regular laser diagnostics at 532 nm. This allows direct investigation of instabilities and plasma dynamics in the stagnated Z pinches. It was found, that the 3D structure of the Z pinch depends on the initial configuration of the wire array [24]. In this section stagnated Z pinches are studied in different wire arrays and compared with data from x-ray imaging diagnostics and spectroscopy. Due to strong shot to shot variations in low wire-number arrays, the pattern of instabilities in different loads is confirmed by statistics of shots.

A. Cylindrical wire arrays

Cylindrical arrays are the most common wire-arrays loads. We tested cylindrical loads with diameters of 3, 8, 12, and 16 mm and wire numbers of 8-16.

Figure 1 presents shadowgrams of the Z pinch produced by implosion of the cylindrical load 16 mm in diameter. The diameter and mass scan of loads at Zebra generator showed that cylindrical arrays Ø16 mm produce an x-ray pulse with smaller energy and power, presumably,

because of the high level of plasma instabilities [18]. Strong plasma perturbations including kink instability and micropinching in these loads were presented in [25]. Figure 1 shows that the pinch has also a loose structure. Shadowgram (a) at the wavelength of 532 nm shows that a significant part of material didn't implode at the maximum of the x-ray pulse. Magnified image (c) taken from the dashed rectangle in shadowgram (b) was lightened to show a loose structure of the stagnated pinch. A small electron density in the pinch of the 16 mm cylindrical arrays is in agreement with previous estimations [13]. An electron density of $N_e = 1.2 \times 10^{20}$ cm^{-3} was derived from analysis of time-integrated Al K-shell spectra. The density measured in 16 mm loads at the Zebra generator with interferometry was $N_e = 0.5 \times 10^{20}$ cm^{-3} [27]. Smaller energy and power of the radiated x-ray pulse measured in [18] can be linked to the bad "quality" of the pinch. Inhomogeneous plasma ablation from wires initiates bubble-like implosion which seeds plasma instability and forms the inhomogeneous pinch. Several sources of implosion inhomogeneity were identified in [12]. First, breaks on the wire core arise stochastically and bubbles start growing at different times. Second, the bubbles accelerate to different speeds. Third, there are wire to wire variations in speed due to variations of electrical contacts with electrodes. Inhomogeneous bubble-like implosion leads to a distribution of material arriving to the axis, with a delay of 15-20 ns from the beginning to the end. A significant part of material is distributed far from the central pinch in the initial volume of the wire array. This can decrease current flowing in the center of the wire array. The central pinch is subjected to strong instabilities and has an inhomogeneous loose structure.

UV shadowgrams and interferograms taken with a field of view of 8 mm at maxima of the x-ray pulses always show wide distribution of non-imploded mass in the initial volume of cylindrical wire arrays 12-16 mm in diameter. However, the stagnated Z pinch from 12 mm cylindrical load is more compact compared to the 16 mm array and presents more pronounced kink instability.

Cylindrical wire arrays 3-8 mm in diameter generate the highest x-ray energy and power at the Zebra generator [18]. It was shown in [25] that strong kink instability and necks 100-150 μm in diameter is typical for 8 mm cylindrical loads. Figure 2 presents images of the stagnated Z pinches from the 8 mm load at 532 nm (a) and 266 nm (b)-(d). Images are taken at the maximum of the generated x-ray pulse (e). Shadowgrams at the wavelength of 532 nm show wide 2.5-3 mm plasma columns with non-imploded peripheral plasma. The UV interferogram and shadowgram unfold the dense pinch inside this column with m=0 and m=1 instabilities and disruption. A differential air-wedge interferometer [31], installed to the UV channel provides a complementary image to the shadowgram. Interferogram indicates plasma in the gap which can support current. Shadowgram (c) was recorded through the slit installed on the CCD camera. The intensity of the UV beam on the slit was enhanced by a factor of 40. The intensity of plasma self-emission and refracted stray rays on the Z pinch image was measured to be < 10% of the intensity of probing radiation passed through the pinch. The magnified image (d) is taken from the rectangle in image (c) and shows a non-symmetrical complicated pattern of the broken stagnated Z-pinch. Small-scale perturbations of plasma are not seen in this image. UV interferogram (b) and shadowgram (b) show steep plasma gradients on the edges of the dense pinch.

The x-ray pulse of the 8 mm cylindrical load has a double-peak shape in diagram (e). Images (a-d) present images at the first peak on the x-ray pulse when material, pushed by implosion bubbles, reach the center and form the dense hot pinch. Laser diagnostics showed that the second

x-ray peak is generated when non-imploded material comes to the center and merges with the main pinch.

Dense Z pinches produced by the 8 mm cylindrical wire arrays have, typically, strong kink and sausage instability at the maximum of the x-ray pulse. Instabilities may be seeded by the implosion bubbles which bring mass, kinetic energy, switch current to the center, and form inhomogeneous pinch at the end of the implosion. Figure 3 (a) shows formation of the dense pinch during the implosion of the 8 mm wire array. Interferogram was taken at 6 ns before the peak of the x-ray pulse. Numbers on the sides of the image mark axial positions of the most pronounced implosion bubbles. Implosion bubbles are partly correlated azimuthally. Formation of the neck on the center of the interferogram clearly correlates with the position of bubble 2. Bubble 1 shows, presumably, a beginning of the neck formation. Bubbles 3 and 4 do not correlate with pronounced necks on the pinch. Therefore, Fig. 3 (a) shows only partial correlation of necks with implosion bubbles. This can be explained by two reasons. First, bubbles reach the center of the array at different times. Some necks may collapse later after the frame presented in Fig. 3. Second, azimuthal correlation of bubbles can be important but Fig. 3 shows the implosion bubbles only in the plane of the image. Results of MHD simulation will be presented below to clarify the role of the implosion bubbles in the development of instabilities in the Z pinch.

The electron density of plasma was measured along the dashed line in Fig. 3 (a). The phase shift φ and density n_e were measured along the implosion bubble (1). The plasma density in the bubble is small. This makes it easy to identify interferometric fringes and measure the plasma density in the close vicinity to the dense pinch. The electron density $n_e(r)$ of plasma in diagram (b) was derived from the phase shift φ (in fringes) using Abel transform:

$$n_e(r) = -\frac{2}{\kappa\lambda}\int_r^R \frac{d\varphi(y)}{dy}\frac{dy}{\sqrt{y^2 - r^2}} \qquad (1)$$

where $\kappa = e^2/m_e c^2$, λ is a wavelength of the probing beam, y is the distance between the ray and the axis of the pinch, and R is the pinch radius. Fringes near the dense pinch are tangled and have a very complicated structure. Two lines in diagram (b) present low and high estimations for the electron density. The non-symmetrical structure of plasma also can add error to processing. The non-transparent zone in the interferogram, 0.8 mm in diameter has an electron density of $N_e > 1.2\text{x}10^{20}$ cm^{-3}. X-ray frame (c) from the time-gated pinhole camera, with resolution of 0.17 mm was taken on the rising edge of the x-ray pulse at the same time as interferogram (a). The Z pinch is already inhomogeneous at the stage of formation at 6 ns before the maximum of the x-ray pulse.

Small diameter cylindrical wire arrays, 1-3 mm in diameter, were investigated in [18]. In small-diameter loads, ablating plasma accumulates in the inner volume much faster than in loads 12-16 mm in diameter. The $\boldsymbol{j}\times\boldsymbol{B}$ force moves the "corona" plasma to the center of the array. The rate of mass ablation per unit length can be calculated with a "rocket" model [8]:

$$\frac{dm}{dt} = \frac{\mu \cdot I^2}{4\pi \cdot V_{abl} \cdot R_0} \qquad (2)$$

where I is the current, R_0 is the radius of the wire array, and V_{abl} is the velocity of the ablating plasma. The ablation rate increases in small-diameter loads as $\sim 1/R$. The inner volume of the cylindrical load depends on the radius like $\sim R^2$. For this reason, small-diameter arrays become opaque for optical laser probing at the wavelength of 532 nm since the ablation phase. Studies

with x-ray pinhole camera [18] showed that loads 1-3 mm in diameter produce Z pinches with multiple bright spots.

UV laser probing clearly shows the internal structure of small-diameter at all stages. Figure 4 presents the stagnated Z-pinch produced by the Ni cylindrical wire array 3 mm in diameter. The dense pinch on shadowgram (a) is a chain of necks and bulges. X-ray pinhole-camera images (a) and (b) present two 3 ns frames in two ranges, E > 0.8 keV (b) and E > 3 keV (c), with a spatial resolution of 0.25mm. X-ray images in both ranges show formation of the inhomogeneous Z pinch with bright spots. We note, that shadowgram (a) and x-ray images (b-2) and (c-2) shows very inhomogeneous Z pinches near the maximum of the generated x-ray pulse.

Figure 5 presents Z pinch from implosion of Al cylindrical wire array 2 mm in diameter. UV two-frame shadowgram (with 5 ns between frames) shows the dynamics of necks and bulges in the stagnated pinch. Circles and rectangles show the same areas in two frames. Areas in circles present development of the break on the neck. Areas in rectangles show formation of the arm which may be a new current path in the vicinity of the neck. The keV x-ray pulse has two peaks due to the two-stage implosion. UV laser frames and x-ray frames (5) from the pinhole camera are timed to the second peak. The Z-pinch observed in shadowgrams is strongly inhomogeneous and distorted by both kink and sausage instabilities. X-ray images (c) show the pinch with numerous bright spots. The rectangle in x-ray frames (4) and (5) identify the area presented in shadowgrams. Magnified images (e) present two x-ray frames in the range of E > 0.8 keV recorded with a resolution of the pinhole camera of 70 μm. The self-radiation x-ray images are blurred due to the long frame duration and a large volume of radiating plasma with different electron temperatures. The angle between UV probing direction and X-ray pinhole images is 22.5°. X-ray images (e) show evolution of bright spots in the area presented in UV shadowgrams (a) and (b). With accuracy of co-alignment of 0.5 mm only a general correlation can be found between shadowgrams and x-ray images. Bright x-ray radiating areas may be linked to necks and fast moving flares on UV images. More precision spatial co-alignment and timing should be installed in future experiments for more accurate identification of bright spots with UV images.

B. Linear (planar) wire arrays

Linear wire array can generate high energy and power [32] and may be applied for ICF fusion research [33]. Plasma bubbles arise on the core breaks and form the implosion pattern in linear loads. Implosion bubbles move from the edge to the next wire in the array and hit the plasma column with a speed up to 250 km/s. Plasma moves from wire to wire toward the center of the array [34]. Due to the strong bubble-like perturbations of the implosion plasma, Z pinches from linear arrays have, typically, an inhomogeneous structure with multiple bright spots.

Linear arrays with 8-12 wire and masses of 46-80 μg/cm were studied for instabilities in the stagnated Z pinch. Figure 6 (a, b) presents two-frame shadowgrams at the wavelength of 266 nm (a, b), with 2.7 ns between frames and at the wavelength of 532 nm (c), with 7 ns between frames. The Z pinch was produced by implosion of the 12-wire linear array. Frames in shadowgram (c) show a wide plasma column of trailing material with m=0 MHD instability and small changes from one frame to another. UV shadowgraphy shows a dense pinch hidden in the trailing plasma. The general structure of the pinch is similar to the structure of the small diameter Ni cylindrical wire array [see Fig. 4 (a)].

The dense pinch consists of a chain of necks and bulges. Necks in frames (a) and (b) stay on the same positions but the structure of necks changes. Implosion in linear arrays starts on edge wires. Implosion bubbles accelerate to a high speed and kinetic energy due to high current and

global magnetic field on the edges. Bubbles break through wires to the center and initiate formation of hot spots on the pinch.

The bulge plasma demonstrated a fast motion at stagnation. Dashed rectangles in two UV frames show plasma moving with a speed of >100 km/s. We note, that plasma motion was also identified in [35] with x-ray spectroscopy. The blue and red Doppler shifts in the pinch plasma were interpreted as a presence of angular motion of plasma. Fast plasma motion at stagnation can produce a Doppler shift of spectral lines and impact measurements of ion plasma temperature.

Arrows in Fig. 6 (b) display plasma jets which move from one bulge to another and create a plasma bridge. This bridge can provide an additional path for current flowing in the neck. Shadowgrams cannot identify current and magnetic fields in plasma but x-ray images (d) deliver additional data. Spatial resolution of pinhole images (d) is 0.25 mm. Two x-ray frames with a 3 ns duration show evolution of bright spots on the pinch. A rectangle in images (d-1) shows the area presented in UV shadowgrams (a) and (b). Several bright spots in frame (d-1) correlate to necks on UV shadowgram (a). The next frame (d-2) shows fading spots compared to frame (d-1). The radiating pinch does not have a core of very bright spots. These changes on the pinch structure may be linked to redistribution of current from necks to trailing plasma and plasma bridges near the necks. The effect of redistribution of current in the pinch was discussed in [36, 37]. A UV Faraday rotation diagnostic is planned for future experiments to clarify the distribution of current in the dense pinch, necks, and trailing plasma.

C. Star wire arrays

Star wire arrays with different configurations were tested in the experiments for instabilities. Optimized star wire arrays radiate short, smooth soft x-ray pulses with the duration of 10-15 ns [13]. During the ablation stage, the wires remain at their initial positions while ablated material streams to the center of the array. The implosion begins when breaks appear on the wire cores and the plasma is accelerated inwards to the array center. In star wire arrays the implosion stage begins with the outer wires and then cascades from wire to wire to the array center [38]. Radiative properties of star loads depend on their diameters, masses, and configuration. Stars with different diameters and configurations were studied and the results are presented below in this section.

As cylindrical loads, large-diameter star arrays radiate x-ray pulses with smaller energy and power and demonstrate high level of plasma instabilities. An inhomogeneous pinch with necks and breaks was observed in [25] with UV shadowgraphy at the maximum of the x-ray pulse. Figure 7 presents Z pinches from two shots with 3-ray 18-wire star loads, 20 mm in diameter, at the later moments. Strong kink instability is seen in interferogram (a) recorded at 10 ns after the maximum of the x-ray pulse. The pinch is split in two arms on the top of the interferogram. Split pinches at stagnation were observed in different types of wire-arrays. Interferometry shows qualitatively that the majority of material has imploded and constricted in the dense pinch with a small amount of trailing plasma. A suggested current path in this pinch is drawn in Fig. 7 (a). This path has an increased length compared to the straight line. Magnified image (b) is taken from the solid rectangle in image (a). Image (b) displays strong plasma gradients on the pinch edge because fringes are not distinguished in the differential shift of the interferogram. A magnified image (c) is taken from the dashed rectangle on the complimentary shadowgram and shows the structure of the neck on the pinch. The neck shows a dense core and a column of the less-density plasma.

A high-resolution UV diagnostic allows investigation of micron-scale plasma instabilities in the stagnated Z-pinch. Density perturbations with a characteristic scale of 10-30 μm were observed in the precursor plasma during formation of the pinch and in the stagnated dense Z-pinch [23]. Figure 7 (b) presents the later stage in the Al 3-ray 18-wire star loads, 20 mm in diameter. A Z-pinch is filled by inhomogeneous plasma and has sharp edges. Plasma perturbations are elongated in one direction with characteristic sizes of (10-30) x (50-200) μm. The structures observed in the Z pinch may be the result of the non-linear evolution of MHD instabilities or development of flute mode instability [39].

Another type of plasma instability in wire-array Z pinches is presented in Figure 8. Interferogram (a) shows a pinch produced by the star load 20 mm in diameter. The pinch is split on two arms. Magnified images (b) and (c) are taken from the dashed and solid rectangular areas in image (a). A shadowgram (d) and magnified image (e) present a pinch from the implosion of the 3-ray star wire array Ø16 mm with 2 mm gates. Loads of these two types are subjected by strong MHD m=0, 1 instabilities at the stagnation phase [23, 24]. Plasma instability with a period of 70 - 270 μm is seen on the edges of the pinches. The pinches have sharp edges in the shadowgram (b) and interferogram (c) in areas of periodic perturbations.

Optimized star wire arrays with masses of 35-45 μg/cm implode to Z pinches with smaller plasma instabilities. Implosion bubbles are mitigated in star arrays during the cascade implosion [11, 38]. These loads generate a powerful short x-ray pulse with duration of 10-12 ns.

UV diagnostics show a smaller level of kink instability in star wire-array Z pinches compared to cylindrical arrays. Figure 9 (a) presents the formation of the pinch during the implosion of 4-ray 24-wire star array at 10 ns before the maximum of the x-ray. Imploding plasma in some areas looks like flares. A dense plasma column of stagnated pinch ~1 mm in diameter is seen in shadowgram (b) later in time, at 5 ns before the maximum of the x-ray pulse. Complementary interferogram (d) shows a small amount of non-imploded and trailed plasma. Kink instability is suppressed but necks on the pinch were seen in other shots with this type of loads. Kink instability and breaks in the pinch develop later and destroy the pinch. X-ray imaging (c) shows a straight plasma column in frame 2 and fast growth of instabilities in frame 3. The stagnated pinch is more homogeneous compared to cylindrical and linear loads but it also has perturbations. Spatial resolution of x-ray images (c) is 0.25 mm. The pinch becomes wider in frame 3, presumably, due to development of the large-scale kink instability. Both UV and x-ray imaging shows the smallest level of plasma instabilities in the pinch at 3-5 ns before the peak of the keV x-ray pulse. The maximum power of soft x-ray radiation is generated by the pinch with plasma instabilities.

The maximum power of Al K-shell keV x-ray radiation is also generated by the pinch with strong plasma instabilities. Light wire arrays with masses of 20-25 μg/cm generate smaller power of soft x-ray but strong radiation in the keV range. Figure 10 presents implosion and the beginning of stagnation in Al 3-ray star wire array with mass of 25 μg/cm. This wire array generates a short 9 ns x-ray pulse in a keV range. A fast growth of instabilities in imploding plasma is seen in shadowgrams (a) and (b). The velocity of leading edges of bubbles is 300 km/s compared to the speed of the main plasma column of 120 km/s. The implosion bubbles seed kink instability during the formation of the Z pinch, as seen in x-ray frames (c). A pinch with strong kink instability exists for ~10 ns and generates the highest power of keV radiation compared to other loads.

IV. 3D MHD simulations of wire-array Z pinches with a Gorgon program

The Z-pinch stagnation stages in the cylindrical and star wire arrays were modeled with the 3D resistive MHD code Gorgon [40, 41]. Simulations were carried out with a spatial grid of 15-30 μm. The distribution of the electron density was integrated along the line of sight. The presentation of simulations with integral $\int N_e dl$ was selected for the better comparison with experimental UV shadowgrams. Simulations with the smallest spatial grid of 15 μm added only small details to patterns of the implosion and stagnation calculated with the 20-30 μm grid. Therefore, the structure of plasma and instability in 3D simulations are well determined and depend on the current pulse and the initial configuration of the wire array. However, the experimental images of the pinches produced by the same type of loads differ due to strong shot to shot variations. Variations in the structure of Z pinches and generated x-ray pulse are initiated by small variations in the current shape and initial conditions in the array (positions of wires, electrical contacts, and other non-reproducible factors). Therefore, only general comparison of instabilities in experimental images with results of simulation was carried out. Below we compared typical plasma structures in stagnated pinches produced by implosion of several types of wire arrays.

A. Simulations of cylindrical wire arrays

Figure 11 displays simulation of the implosion and stagnation in the Al cylindrical wire array, 12 mm in diameter, driven by the typical Zebra 1 MA current pulse. Simulations display side-on (a-c) and end-on views on the Z pinch at several moments. The timing diagram explains positions of frames to the current and synthetic x-ray pulse. The Z pinch is very inhomogeneous at the beginning of the x-ray pulse in frame (a) and has areas with small plasma density. Image (a) presents a large amount of non-imploded material near the pinch. Strong kink instability rises in the pinch in frame (b) and destroys the pinch in frame (c). End on frames (d-f) also show non-imploded material distributed in the initial volume of the wire array. We note that a loose structure of the stagnated pinch and large amount of non-imploded material was observed in implosions of cylindrical wire arrays with diameters of 12-16 mm. Frames (a-c) display a status of the Z-pinch at the maximum of the x-ray pulse in diagram (i). The long 35 ns x-ray pulse in (i) is typical for experimental pulse shapes in large-diameter cylindrical loads and can be explained by the long and temporally inhomogeneous implosion.

Simulations of the implosion and stagnation stages in cylindrical loads 8 mm in diameter were carried out in [25] with grids of 20-30 μm. Simulations of 3D density profiles in Z pinches displayed strong kink instability developing at the maximum of the x-ray pulse. Only a quarter of the current is flowing through the dense plasma pinch at stagnation. The electron temperature of the Z pinch varied from 100 eV in large cold areas up to 1 keV in some hot spots [25].

Figure 12 display mass plasma density in the Z pinch integrated along the line of sight. The role of implosion bubbles can be analyzed from these images. The most pronounced implosion bubbles are marked by dashed lines and numbers at the right side of image (d). Images (b-d) show development of strong kink instabilities with necks and breaks in the areas of bubbles on the main pinch. Kink instability in frame (c) [see dashed lines (1) and (4)] produces breaks on next frame (d). Breaks in frame (c) [see dashed lines (2) and (3)] merge later in frame (d). Therefore, the implosion bubbles initiate areas of instabilities on the stagnated pinch which can exist >15 ns. Experiments confirm correlation of positions of necks on the pinch with bright spots on the x-ray images. Laser imaging provides evidences of initiation of necks by the

implosion bubbles. X-ray images show that bright spots on the Z pinches radiate during 20 ns [18].

Simulations show that the maximum of the x-ray pulse is generated in cylindrical wire arrays by the pinch subjected to strong instabilities. This point is also in agreement with experimental data delivered by UV probing diagnostics.

Bubble-like implosion is a result of the "fundamental" instability during the ablation stage [12]. The bubble-like implosion depends on the wire number, see Fig. 13 (a) and (b). In small wire-number arrays implosion bubbles rise at different time and can accelerate to the speed of 500 km/s [6]. First-born bubbles have the highest speed and can suppress the development of latter bubbles. Development and merging of bubbles is seen in Fig. 13 (c) and (d). Final bubbles have a larger axial scale with a period of 1-2 mm. Bubbles bring current and kinetic energy to the axis of the array and initiate formation of necks on the pinch. The bubble-like beginning of implosion is more homogeneous in the 32-wire array, as it shown in Fig. 13 (b), (see also Ref. [42]). Magneto-Rayleigh-Taylor instability increases initial inhomogeneity of the imploding plasma.

B. Simulations of star wire arrays

Mitigation of implosion bubbles during the cascade implosion was demonstrated in star wire arrays [13]. Three-dimensional Gorgon simulations also show the formation of straight pinch in a four-ray 24-wire star array. Simulation of the cascading implosion is shown in Fig. 14 (a-c). Implosion from the edge wires cascade from wire to wire and produce plasma columns near positions of internal wires (c). Simulation displays the higher level of instability compared to experiments. One bubble on the center broke the plasma column and reached the axis of the array. This bubble initiates a disruption on the pinch, as seen in frames (d) and (f). Frame (d) shows the formation of the pinch with flares which are also seen in Fig. 9 (a). A straight dense Z-pinch plasma column with small kink instability forms in the next frame (f) at the maximum of the x-ray pulse. These implosion and stagnation dynamics are in agreement with experimental observations. The last frame (g) in Fig. 14 shows fast grows of kink instability. Current in the helical components generates regions of the axial magnetic field which force an expansion of kink instability. Fast grows of the amplitude of m=1 instability and expansion of the pinch was observed in time-gated x-ray images of star wire arrays. Fast grows of instability destroys the pinch and "cut" a tail on the x-ray pulse.

V. Extraction of plasma parameters with x-ray spectroscopy

The electron temperature and density of Z-pinch plasmas were extracted from analysis of Al x-ray K-shell spectra. The temperature of bright areas on spectra of cylindrical load Ø8 mm was measured in the range of 400-450 eV while that of low intensity areas was of 320-360 eV [25]. In this section, we discuss plasma parameters inferred from the analysis of spatially-resolved spectra recorded along the Z pinch axis produced in the implosion of an Al cylindrical load of 3 mm in diameter.

X-ray spectra were recorded by a time-integrated spectrometer with a convex KAP crystal [18] on BIOMAX-MS film [43]. Spatial resolution of spectra along the pinch axis was 0.46 mm. The spectral range of observation was 5-10 Å. Experimental Al K-shell spectra were analyzed using a collisional-radiative atomic kinetics code PrismSPECT taking into account the effects of

radiation transport in the level population kinetics [44]. The issue of this analysis is a complicated 3D structure and temporal dynamics of the plasma which are averaged by the time-integrated spectrometer over an area of >0.5 mm. Therefore, only time-averaged analysis of plasma parameters can be performed. Several spatially-resolved spectra were processed for each shot. Figure 14 displays spectrum (a) from the Al cylindrical wire array, 3 mm in diameter, x-ray frames from the pinhole camera (b), and comparisons of experimental and theory spectra (c-d). Spectrum (a) has areas of high, medium, and small intensity. Some areas of spectrum are distorted by strong kink instability. Spectra were selected in areas shown by dashed lines and numbers in Fig. 14 (a). A spectral range of 5.4-6.9 Å was selected for comparison of experimental and calculated K-shell spectra. This range includes Heβ - Heε lines, Lyβ - Lyδ lines, He- and Li-like satellites, and H- to He-like Al radiative recombination emission. Hence, with similar type of transitions across three ionization stages, the spectra have significant electron temperature sensitivity for spectroscopy diagnostic. Al Heα and Lyα lines were excluded from the analysis due to strong saturation of film. Simulations were fitted to experimental spectra using a minimization procedure. Figure 15 (c) and (d) show fitting of spectral plots along line (a1) with a bright spot and the area with small intensity along line (a2). The spectrum in the area of bright spot (a1) is characteristic of an electron temperature and density of T_e = 430 eV and N = 3x10^{20} mg/cm^3, respectively. Spectrum in the area of low intensity (a2) is characteristic of an electron temperature of less than T_e = 270 eV, and the H-like lines are significantly weak compared to those in (a1). Comparison of positions of hot area (a1) in spectra with x-ray frames (b) shows that the hot area correlates with the positions of bright spots in x-ray images (b1) - (b4). Spectrum (a2) correlates with low-intensity areas between two hot spots in frames (b1)-(b3) and with a bright area in frame (b4). Therefore, spectrum (a2) accumulates radiation from cold areas during 20 ns and adds radiation from the hotter plasma in frame (b4). The bright pinch in the top of frame (b4) is timed at the x-ray burst at the end of the keV x-ray pulse (2), as seen in diagram (e). The Z pinch radiates during >30 ns. X-ray images present a straight plasma pinch during 20 ns which then fades in frame (b3). The pinch burns up again in frame (b4) but m=0 and m=1 plasma instabilities also rise fast. Kink instability destroys the pinch in latter frame, not shown in Fig. 15. Comparison of x-ray frames (b) with spectra (a) confirms that time-integrated spectra represent radiation emitted from plasmas with different temperatures, densities, and evolution. A contribution of cold long-living plasma to the spectra can be comparable to the contribution of hot short-living spots. Measurement of plasma parameters in other plots on spectrum (a) yield electron temperature ranges of 390-440 eV in hot areas and 270-320 eV in cold areas.

VI. Discussions

UV diagnostics at the wavelength of 266 nm unfolds small-scale instabilities in the dense Z pinch hidden in the wide column of trailing material. Imaging diagnostics show that wire array Z pinches carry a strong signature of the initial configuration of the load plasma dynamics at the ablation and implosion stages. A 3D structure of the stagnated pinch and a pattern of instabilities differ in linear arrays, stars, and cylindrical wire arrays. Cylindrical wire arrays with different diameters produce Z pinches of different types. 3D MHD modeling can reproduce a general pattern of instabilities typical for different wire arrays. The 3D Gorgon resistive MHD modeling is in a good agreement with implosion and stagnation scenarios observed in very different star-like, linear, and cylindrical wire arrays. This creates an opportunity to study Z pinch using both

experimental and simulation data. MHD simulations display 3D evolution of wire array at all stages with a spatial grid of up to 15 μm. Experimental data provides discrete frames of stagnated Z pinches from laser and x-ray imaging with spatial and temporal resolution limited by diagnostics. Shot-to-shot variations are important but statistics based on observations from more than 70 shots with different wire arrays help to establish general regularity in plasma patterns. Systematic comparisons of simulation and data can be used for analysis of implosion and stagnation dynamics and development of instabilities.

Simulations and experiments show that implosion bubbles play a crucial role in formation of points of instability on the pinch during implosion. Bubbles initiate development of m=0, 1 instabilities which create later breaks on the pinch. Bubbles-like inhomogeneity can be mitigated in star wire arrays with optimal mass and configuration during cascade implosion. In linear arrays bubbles arising on the edge wires have high velocity due to the strong [**j**x**B**] force [34]. They punch the next wires and move to the center instead of the regular cascading process. The formation of bubbles is similar to implosion in low wire-number arrays with high current in each wire. Bubbles bring material and switch current to the center and initiate generation of the x-ray pulse. Strong bubble inhomogeneity was also observed in implosions of small diameter wire arrays [18]. Necks on the Z pinch generate bright spots which are seen in x-ray images as bright spots. Kink instability also develops on these points. Finally, instabilities break the pinch.

The implosion dynamic is predetermined by the wire array configuration, therefore, stagnated Z pinches has specific features. Cylindrical wire arrays implode to Z-pinches with strong m=0 and m=1 plasma instabilities and bright spots on x-ray images. Kink and sausage instabilities are always seen at the maximum of the x-ray pulse and even on its rising edge. We note that the observed pattern is far from a textbook MHD instability due to chaotic and random motion with the non-coherent features. Micropinches 60-150 μm in diameters were observed in shadowgrams and simulations. Large diameter non-optimal arrays implode to the inhomogeneous pinch with a loose structure and small plasma density. Loads with diameters of 5-8 mm generate the x-ray pulse with higher power and energy. Compact loads with diameters of 2-3 mm generate long high-energy 30-35-ns x-ray pulses. Numerical necks produce a chain of bright spots along the pinch. Linear-array Z pinches also demonstrate a “bulge - neck” periodical structure with bright spots. Optimized star arrays implode to a straight Z pinch with a much smaller amount of trailing material compared to compact and linear wire arrays.

Strong instabilities were observed in cylindrical, linear, and non-optimized star wire arrays at the maximum of the generated x-ray pulse. Z pinches with strong instabilities can exist and radiate during tens of nanoseconds. X-ray energy generated by small-diameter cylindrical and linear wire arrays is significantly higher than available kinetic energy of implosion [18, 32]. Compact cylindrical wire array 2-3 mm in diameter begins to radiate when bubbles deliver material to the center of the array. A significant part of wire array material is not imploded at that time. This material implodes later at the stagnation stage. The trailing mass can provide an alternative path for the current but MHD simulations display a drop of conductivity in the non-imploded peripheral plasma [45]. We suggest that the first x-ray burst with power of 0.3-0.5 TW ionizes peripheral plasma in the volume of the small-diameter array [46]. PrismSpect simulations were carried out to estimate energy absorbed in trailing material during the x-ray burst. The Z pinch was modeled by a plasma column 1 mm in diameter with an electron temperature of 400 eV. The calculated radiative energy of this plasma column exceeds experimental radiative energy by a factor of 6. This is in a general agreement with 3D MHD Gorgon simulations which show that the surface associated with high-temperature plasma occupies only a small part of the Z

pinch [see Figure 4(e) in Ref. 25]. So, the effective surface of the pinch was decreased by the factor of 6 to meet real radiation energy. Next, absorption of Z-pinch radiation in the non-imploded peripheral plasma with an electron temperature of 5 eV was calculated using the PrismSpect code. Calculations show that >30% of Z-pinch radiation can be absorbed in the peripheral material thus raising its temperature to 20-50 eV which results in a plasma conductivity increase by a factor of 10-20. The second implosion of the trailing mass can produce the second x-ray burst (see Figures 2 and 6 and References [42, 47]) or support generation of the long x-ray pulse in compact wire arrays. The pressure of the imploding plasma can temporally stabilize the stagnated Z-pinch with strong instabilities and prolong generation of the high power x-ray pulse. Several mechanisms may provide enhanced heating of plasma: **j**x**B** - forced expansion of the m=1 helix [40], pdV compressional work, high resistivity due to the strong plasma inhomogeneity, and longer current path in the pinch. The Z pinches demonstrate a fast plasma motion with velocity of 100 km/s at stagnation. Gorgon simulations also display fast plasma dynamics of the stagnated pinch. A stagnated Z pinch is a source of kinetic energy which may be built from magnetic energy through plasma instabilities. Physical mechanisms of conversion of magnetic energy will be studied in future experiments and simulations. Experiments show that high-power keV x-ray pulses are also generated by the pinch with strong instabilities.

In star wire arrays the cascade implosion snowplows a majority of plasma to the main pinch. With the absence of trailing mass, plasma instabilities grow fast and destroy the pinch. This could explain the short duration of the x-ray pulse generated by star arrays. The dynamic of stagnation in stars support suggestion about the role the prolonged implosion and trailing mass for generation of the long pulse in small-diameter and linear wire arrays.

Presented experiments and data about instabilities in the stagnation Z pinches were carried out at the 1 MA Zebra generator. Strong implosion inhomogeneity and hot spots on the pinch were observed in other pulsed power generators with current of 1-20 MA [17, 48]. UV laser probing may be applied to Z pinches at multi-MA generators to study plasma instabilities and enhanced x-ray radiation [49].

Acknowledgements

The authors thank Drs. A. M. Covington and V. Davis for support and A. L. Astanovitskiy, O. Dmitriev, V. Nalajala, and B. Talbot for help with experiments and data processing. This work was supported by DOE/NNSA under the UNR grants DE-FC52-06NA27616 and DE-SC0008824.

References

1. R. B. Spielman, C. Deeney, G. A. Chandler, M. R. Douglas, D. L. Fehl, M. K. Matzen, D. H. McDaniel, T. J. Nash, J. L. Porter, T. W. L. Sanford, J. F. Seaman, W. A. Stygar, K. W. Struve, S. P. Breeze, J. S. McGurn, J. A. Torres, D. M. Zagar, T. L. Gilliland, D. O. Jobe, J. L. McKenney, R. C. Mock, M. Vagras, T. Wagoner, Phys. Plasmas **5**, 2105 (1998).
2. C. Deeney, M. R. Douglas, R. B. Spielman, T. J. Nash, D. L. Peterson, P. L'Eplattenier, G. A. Chandler, J. F. Seamen, K. W. Struve, Phys. Rev. Lett. **81**, 4883 (1998).
3. M. E. Cuneo, E. M. Wasiman, S. V. Lebedev, J. P. Chittenden, W. A. Stygar, G. A. Chandler, R.A. Vesey, E. P. Yu, T.J. Nash, D.E. Bliss, G.S. Sarkisov, T.C. Wagoner, G.R. Bennett, D. B.

Sinars, J.L. Porter, W.W. Simpson, L.E. Ruggles, D.F. Wenger, C.J. Garasi, B. V. Oliver, R. A. Aragon, W. E. Fowler, M. C. Hettrick, G. C. Idzorek, D. Johnson, K. Keller, S.E. Lazier, J.S. McGurn, T.A. Mehlhorn, T. Moore, D.S. Nielsen, J. Pyle, S. Speas, K.W. Struve, and J.A. Torres, Phys. Rev. E **71**, 046406 (2005).
4. W. A. Stygar, M. E. Cuneo, R. A. Vesey, H. C. Ives, M. G. Mazarakis, G. A. Chandler, D. L. Fehl, R. J. Leeper, M. K. Matzen, D. H. McDaniel, J. H. McGurn, J. L. McKenney, D. J. Muron, C. L. Olson, J. L. Porter, J. J. Ramirez, J. F. Seamen, C. S. Speas, R. B. Spielman, K. W. Struve, J. A. Torres, and E. M. Waisman, T. C. Wagoner and T. L. Gilliland, Phys. Rev E **72**, 026404 (2005).
5. B. A. Remington, R. P. Drake, D. D. Ryutov, Rev. Mod. Phys. **78**, 755 (2006).
6. M. G. Haines, Plasma Phys. Control. Fusion **53,** 093001 (2011).
7. D. D. Ryutov, M. S. Derzon, and M. K. Matzen, Rev. Mod. Phys. **72**, 167 (2000).
8. S. V. Lebedev, F. N. Beg, S. N. Bland, J. P. Chittenden, A. E. Dangor, M. G. Haines, K. H. Kwek, S. A. Pikuz,T. A. Shelkovenko, Phys. Plasmas **8**, 3734 (2001).
9. S. V. Lebedev, D. J. Ampleford, S. N. Bland et al., Plasma Phys. Contr. Fusion **47,** A91 (2005).
10. B. Jones, C. Deeney, J. L. McKenney, C. J. Garasi, T. A. Mehlhorn, A. C. Robinson, S. E. Wunsch, S. N. Bland, S.V. Lebedev, J. P. Chittenden, S. C. Bott, D. J. Ampleford, J. B. A. Palmer, J. Rapley, G. N. Hall, B.V. Oliver, Phys. Rev. Lett. **95**, 225001 (2005).
11. D. B. Sinars, D. B. Sinars, M. E. Cuneo, B. Jones, C. A. Coverdale, T. J. Nash, M. G. Mazarakis, J. L. Porter, C. Deeney, D. F. Wenger, R. G. Adams, E. P. Yu, D. E. Bliss, G. S. Sarkisov, Phys. Plasmas **12**, 056303 (2005).
12. V. V. Ivanov, V. I. Sotnikov, G. S. Sarkisov, T. E. Cowan, S. N. Bland, B. Jones, C. A. Coverdale, C. Deeney, P. J. Laca, A. L. Astanovitskiy, A. Haboub, Phys. Rev. Lett. **97**, 125001 (2006).
13. V. V. Ivanov, V. I. Sotnikov, A. Haboub, A. P. Shevelko, A. L. Astanovitskiy, A. Morozov, E. D. Kazakov, S. D. Altemara, Phys. Rev. Lett. **100**, 025004 (2008).
14. J. P. Friedberg, Rev. Mod. Phys. **54**, 801 (1982).
15. P. G. Burkhalter, C. M. Dozier, D. J. Nagel, Phys. Rev. A **15**, 700 (1977).
16. N. R. Pereira, J. Davis, J. Appl. Phys. **64**, R1 (1988).
17. J. P. Apruzese, J. W. Thornhill, A. L. Velikovich, B. Jones, D. J. Ampleford, C. A. Coverdale, "Diagnosing plasma conditions in copper wire array shots on Z: spatially averaged analysis compared to inferred properties of individual bright spots", Bull. APS **55**, No. 15, 92 (2010).
18. V. V. Ivanov, V. I. Sotnikov, J. M. Kindel, P. Hakel, R. C. Mancini, A. L. Astanovitskiy, A. Haboub, S. D. Altemara, A. P. Shevelko, E. D. Kazakov, P. V. Sasorov, Phys. Rev. **E** 79, 056404 (2009).
19. B. Jones, C. Deeney, C. A. Coverdale, C. J. Meyer, P. D. LePell, IEEE Trans. Plasma Sci. **34**, 213 (2006).
20. D. H. Kalantar, D.A. Hammer, Phys. Rev. Lett. **71**, 3806 (1993).
21. S. A. Pikuz, D. B. Sinars, T. A. Shelkovenko, K. M. Chandler, D. A. Hammer, G. V. Ivanenkov, W. Stepniewski, and I. Yu. Skobelev, Phys. Rev. Lett., **89**, 035003 (2002).
22. S. A. Pikuz, T. A. Shelkovenko, D. B. Sinars, J. B. Greenly, Y. S. Dimant, D. A. Hammer, Phys. Rev. Lett., **83**, 4313 (1999).
23. S.V. Lebedev, F. N. Beg, S. N. Bland, J. P. Chittenden, A. E. Dangor, M.G. Haines, S. A. Pikuz, T. A. Shelkovenko, Phys. Rev. Lett. **85**, 98 (2000).

24. D. B. Sinars, G. R. Bennett, D. F. Wenger, M. E. Cuneo, J. L. Porter, Appl. Opt. **42**, 4059 (2003).
25. V. V. Ivanov, J. P. Chittenden, S. D. Altemara, N. Niasse, P. Hakel, R. C. Mancini, D. Papp, A. A. Anderson, Phys. Rev. Lett. **107**, 165002 (2011).
26. A. I. Velikovich, J. Davis, J. W. Thornhill, and J. L. Giuliani, Jr., L. I. Rudakov, C. Deeney, Phys. Plasmas **7**, 3265 (2000).
27. G. S. Sarkisov, S. E. Rosenthal ,K. W. Struve V. V. Ivanov, T. E. Cowan, A. Astanovitskiy, A. Haboub, Phys. Plasmas **14**, 052704 (2007).
28. V. V. Ivanov, A. L. Astanovitskiy, D. Papp, J. P. Chittenden, S. N. Bland, B. Jones, S. D. Altemara, Phys. Plasmas **17**, 102702 (2010).
29. V. V. Ivanov, S. D. Altemara, A. L. Astanovitskiy, G. S. Sarkisov, A. Haboub, D. Papp, J. M. Kindel, IEEE Trans. Plasma Sci. **38**, 574 (2010).
30. V.V. Ivanov, G. S. Sarkisov, P. J. Laca, V. I. Sotnikov, V. L. Kantsyrev, B. Jones, C. A. Coverdale, P. D. LePell, C. Deeney, K. W. Struve, A. L. Astanovitskiy, D. Fedin, B. Le Galloudec, V. Nalajala, I. Shrestha, T. E. Cowan, IEEE Trans. Plasma Sci. **34**, 2247 (2006).
31. G. S. Sarkisov, Instrum. Exp. Tech. **39**, 727 (1996).
32. V. Kantsyrev, A. Safronova, D. Fedin, V. Ivanov, A. Esaulov, V. Nalajala, I. Shrestha, S. Pokala, K. Williamson, N. Ouart, F. Yilmaz, P. Laca, T. E. Cowan, L. I. Rudakov, B. Jones, C.A. Coverdale, C. Deeney, P. D. LePell, A. L. Velikovich, A. S. Chuvatin, IEEE Trans. Plasma Sci. **34**, No. 2, 194 (2006).
33. B. Jones, D. J. Ampleford, R. A. Vesey, M. E. Cuneo, C. A. Coverdale, E. M. Waisman, M. C. Jones, W. E. Fowler, W. A. Stygar, J. D. Serrano, M. P. Vigil, A. A. Esaulov, V. L. Kantsyrev, A. S. Safronova, K. M. Williamson, A. S. Chuvatin, and L. I. Rudakov, Phys. Rev. Lett. **104**, 125001 (2010).
34. V. V. Ivanov, V. I. Sotnikov, A. Haboub, G. E. Sarkisov, R. Presura, T. E. Cowan, Phys. Plasmas **14**, 032701 (2007).
35. S. A. Pikuz, J. D. Douglass, T. A. Shelkovenko, D. B. Sinars, D. A. Hammer, Rev. Sci. Instrum. **79**, 013106 (2008).
36. P. V. Sasorov, Sov. J. Plasma Phys. **18**, 143 (1992).
37. G. E. Sarkisov, A. S. Shikanov, B. Etlicher, S. Attelan, C. Rouille, V. V. Yan'kov, JETP **81**, 743 (1995).
38. A. Haboub, V.V. Ivanov, A. L. Astanovitskiy, A. A. Morozov, S. D. Altemara, IEEE Trans. Plasma Sci. **36**, 1290, (2008).
39. V.V. Ivanov, V. I. Sotnikov, T. E. Cowan, P. J. Laca, A. L. Astanovitskiy, B. Le Galloudec, G. S. Sarkisov, B. Jones, C. Deeney, B. V. Oliver, T. A. Mehlhorn, J. N. Leboeuf, IEEE Trans. Plasma Sci. 35, 1170 (2007).
40. J. P. Chittenden, S. V. Lebedev, C. A. Jennings et al., Plasma Phys. Control. Fusion **46,** B457 (2004).
41. J. P. Chittenden, C. A. Jennings, Phys. Rev. Lett. **101**, 055005 (2008).
42. S. N. Bland, S. V. Lebedev, J. P. Chittenden, G. N. Hall, F. Suzuki-Vidal, D. J. Ampleford, J. B. A. Palmer, S. A. Pikuz, T. A. Shelkovenko, Phys. Plasmas **14**, 056315 (2007).
43. F. J. Marshall, J. P. Knauer, D. Anderson, and B. L. Schmitt, Rev. Sci. Instrum. **77**, 10F308 (2006).
44. J. J. MacFarlane, I. E. Golovkin, P. Wang, P. R. Woodruff, N. A. Pereira, High Energy Density Phys. **3**, 181 (2007).

45. C. A. Jennings, M. E. Cuneo, E. M. Waisman, D. B. Sinars, D. J. Ampleford, G. R. Bennett, W. A. Stygar, and J. P. Chittenden, Phys. Plasmas **17**, 092703 (2010).
46. P. V. Sasorov (private communication).
47. S. V. Lebedev, D. J. Ampleford, S. N. Bland, S. C. Bott, J. P. Chittenden, J. Goyer, C. Jennings, M. G. Haines, G. N. Hall, D. A. Hammer, J. B. A. Palmer, S. A. Pikuz, T. A. Shelkovenko T. Christoudias, Plasma Phys. Control. Fusion **47,** A91 (2005).
48. D. B. Sinars, M. E. Cuneo, E. P. Yu, D. E. Bliss, T. J. Nash, J. L. Porter, C. Deeney, M. G. Mazarakis, G. S. Sarkisov, D. F. Wenger, Phys. Rev. Lett. **93**, 145002 (2004).
49. D. B. Sinars, R. W. Lemke, M. E. Cuneo, S. V. Lebedev, E. M. Waisman, W. A. Stygar, B. Jones, M. C. Jones, E. P. Yu, J. L. Porter, D. F. Wenger, Phys. Rev. Lett. **100**, 145002 (2008).

Fig. 1. (Color online) Shadowgrams (a)-(c) present a central part of the pinch at the wavelengths of 532 nm (a) and 266 nm (b, c). UV image (b) presents the area from the rectangle in image (a). The Z-pinch is produced by the implosion of a cylindrical 8-wire array 16 mm in diameter with a mass of 37 μg/cm, shot 2355. The diagram (d) presents the timing of the frame at 532 nm (diamond), 266 nm (arrow), current (1) and keV x-ray pulse (2).

Fig. 2. (Color online) Shadowgrams (a, c) and interferogram (b) of the of the Z pinch at the wavelengths of 532 nm (a) and 266 nm (b). UV interferogram (b) presents a rectangular area in image (a). The rectangular area in UV shadowgram (c) is presented in the magnified image (d). The Z-pinch is produced by the implosion of the Al cylindrical 16-wire array 8 mm in diameter with a mass of 53 μg/cm, shot 2375. The diagram (e) presents the timing of the frame at 532 nm (diamond) and 266 nm (arrow) to the current (1) and x-ray pulses (2).

Fig. 3. (Color online) (a) Interferogram at 266 nm of the Z pinch during the implosion of the Al cylindrical 12-wire array Ø8 mm, shot 2711, with mass of 25 μg/cm. (b) A diagram of the electron density calculated along the dashed line on (a). A dashed rectangle in the diagram shows a non-transparent zone. Two lines in the diagram present low and high estimations for the electron density. (c) X-ray 3 ns frame from the pinhole camera filtered for E > 3 keV and timed to image (a).

Fig. 4. (Color online) Shadowgram at 266 nm (a), x-ray pinhole images at ranges E > 0.8 keV (b) and E > 3 keV (c), and timing diagram (d) from the Ni cylindrical 12-wire array Ø3 mm, shot 2543, with mass of 49 μg/cm. The diagram (d) presents the timing of the shadowgram at 266 nm (arrow) and x-ray frames (stripes) to the current (1) and x-ray pulses (2).

Fig. 5. (Color online) Two-frame shadowgram at 266 nm (a, b), pinhole x-ray frames (c), and a timing diagram (d) from the implosion of the Al cylindrical 8-wire array Ø2 mm, with mass of 37 μg/cm (shot 2661). Six 3-ns x-ray frames (c) with 6 ns between frames are taken in the range E > 3 keV (the upper row) and E > 0.8 keV (the bottom row). Magnified images (e) present rectangular areas from frames (4) and (5) in image (c). The timing diagram (d) presents a current (1) and x-ray (2) pulses, two UV frames (arrows), and six x-ray frames (stripes).

Fig. 6. (Color online) Shadowgrams at 266 nm (a, b) and 532 nm (c), x-ray pinhole frames at E > 3 keV (c), and a timing diagram (d) from implosion of the Al linear 12-wire 10 mm array, with mass of 47 μg/cm, shot 2544. The delay between frames (a) and (b) is 2.7 ns, 7 ns between frames (c), and 6 ns between x-ray images (d). The diagram (d) presents the timing of the shadowgrams at 266 nm (arrows), at 532 nm (dimonds), and x-ray frames (stripes) to the current (1) and x-ray pulses (2).

Fig. 7. (Color online) Interferogram (a) and shadowgram (d) at 266 nm from shots 2371 and 2367 present Z-pinches produced by implosions of the Al 3-ray 18-wire star loads, 20 mm in diameter with masses of 60 μg/cm. Image (a) is taken 10 ns after the maximum of the x-ray pulse and image (d) shows time 24 ns after the maximum. A magnified image (b) is taken from the dashed rectangle in interferogram (a). A magnified image (c) is taken from the complimentary shadowgram and the solid rectangle in interferogram (a) shows a position of image (c). A false-color image (e) is taken from the rectangle in shadowgram (d).

Fig. 8. (Color online) Interferogram at the wavelength of 266 nm (a) and magnified images (b, c) from the dashed and solid rectangles present a Z-pinch produced by the Al 3-ray 18-wire star array Ø20 mm, m = 60 μg/cm, shot 2351. (d) Shadowgram of Al 15-wire 3-ray star Ø16 mm, m = 45 μg/cm, shot 2189. An interferogram (e) presents the area from the dotted rectangle in (d). Images are taken 7 ns before (a) and 28 ns after (b) the maximum of the x-ray pulse.

Fig. 9. (Color online) Shadowgrams (a, b) and interferogram (d) at 266 nm and x-ray frames at E > 3keV (c) present Z-pinches produced by implosions of two Al 4-ray 24-wire star loads, 16 mm in diameter, with masses of 50 μg/cm, shots 2348 (a) and 2346 (b-d). UV images are taken at 10 ns (a) and 5 ns (b) before the maximum of the x-ray pulse. X-ray timing to the x-ray pulse is -13 ns (1), -6 ns (2), and 0 ns (3).

Fig. 10. (Color online) Two-frame shadowgram at 532 nm (a, b) and two x-ray frames at E > 3keV (c) present implosion and stagnation in Al 3-ray 12-wire star arrays with m = 25 μg/cm. Shadowgrams (shot 993) are taken at 15 ns (a) and 8 ns (b) before the maximum of the x-ray pulse. Dotted lines show a center of the array. Dashed lines show initial positions of wires. Diagram (d) shows timing of x-ray frames (stripes) to the x-ray pulse (1) and current pulse (2) in shot 2820.

Fig. 11. (Color online) 3D MHD Gorgon simulation of the mass density integrated along the line of sight, in the cylindrical wire array Ø12 mm. (a-c) Side-on view. (d-g) End-on view. (i) The timing diagram with a current pulse (1) and calculated x-ray pulse (2).

Fig. 12. (Color online) 3D MHD Gorgon simulation of the mass density integrated along the line of sight, in the cylindrical wire array Ø8 mm. (a-d) Side on views with timing of frame to the maximum of the x-ray pulse of -25 ns (a), -15 ns (b), -10 ns (c), and 0 ns (d).

Fig. 13. (Color online) (a, b) Implosion bubbles in Al cylindrical arrays Ø16mm with 8-wires (a) and 24 wires (b), shots 512 and 663. (c, d) Two frames of shadowgraphy, with 7 ns between frames, shows merging of two bubbles along the dotted line in the Cu 4-wire array, shot 552.

Fig. 14. (Color online) (a-c) 3D MHD Gorgon simulation of the mass density integrated along the line of sight, in the 4-ray 24-wire star array Ø16 mm. Maximum of the synthetic x-ray pulse is at 172 ns.

Fig. 15. (Color online) (a) K-shell time-integrated spectrum of the Al cylindrical load Ø3 mm, shot 2704. (b) Time-gated x-ray images of this pinch with a frame duration of 3 ns and delay between frames of 6 ns. (c) and (d) Experimental spectra from plasma regions 3 and 2, indicated with arrows, and spectra computed with PrismSpect (triangles). (e) The timing diagram with a current pulse (1), x-ray pulse (2), and four x-ray frames on the top of the diagram. (f) Directions to the spectrometer and pinhole camera.

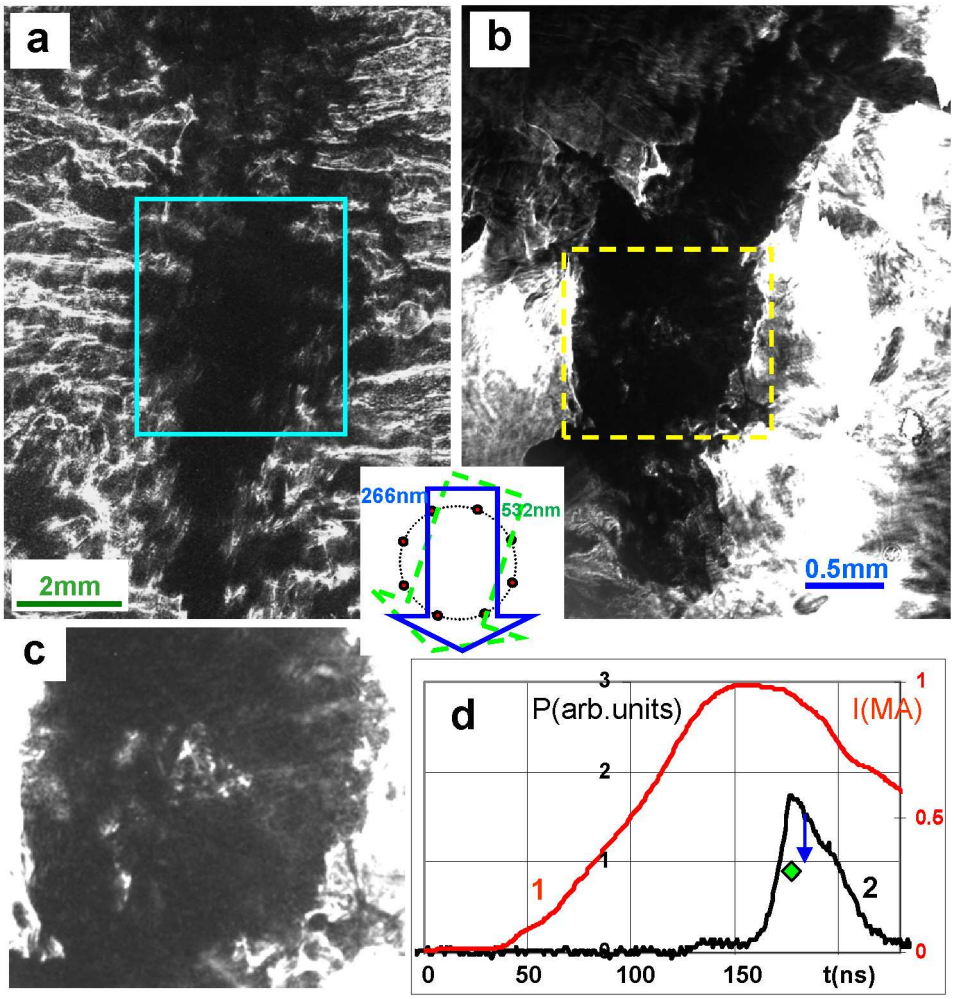

Figure 1 EU11001 01OCT2012

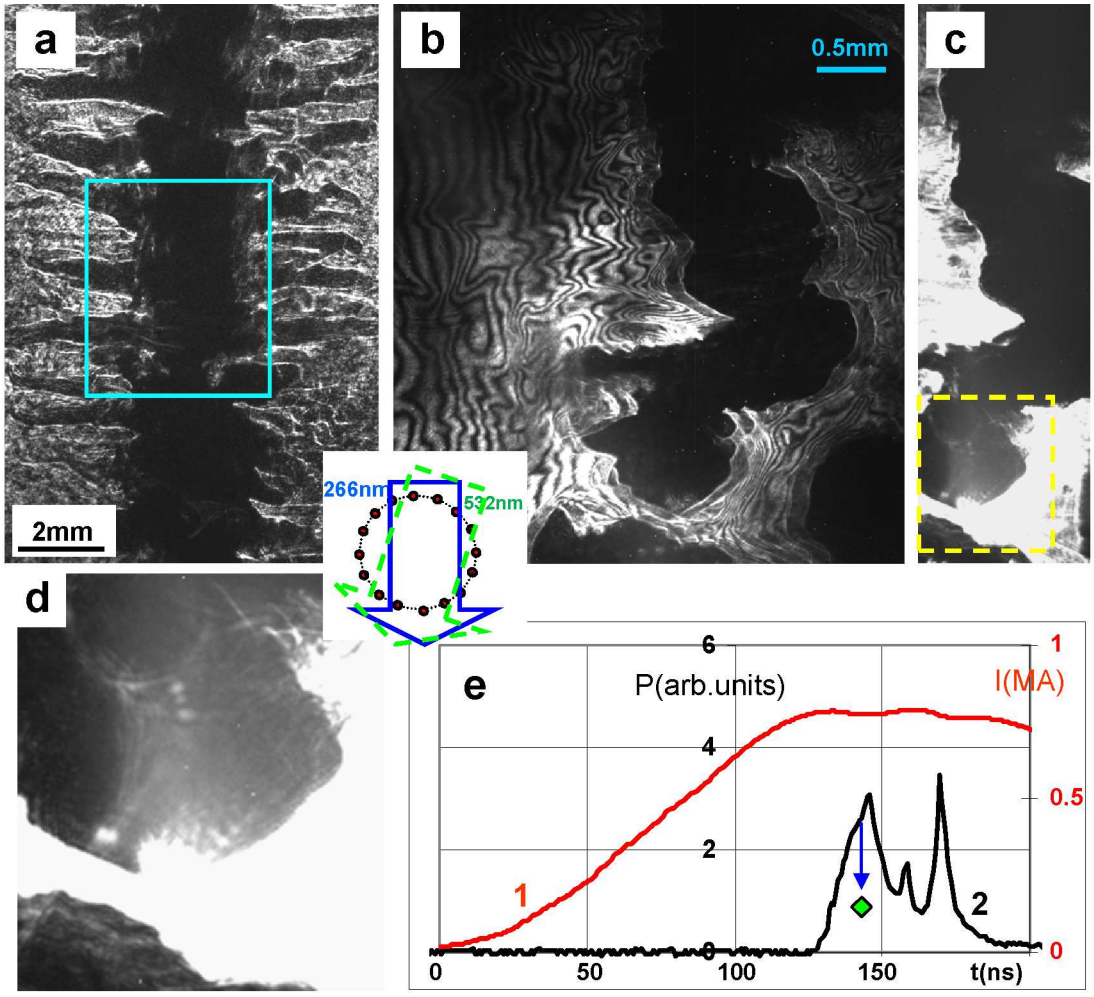

Figure 2 EU11001 01OCT2012

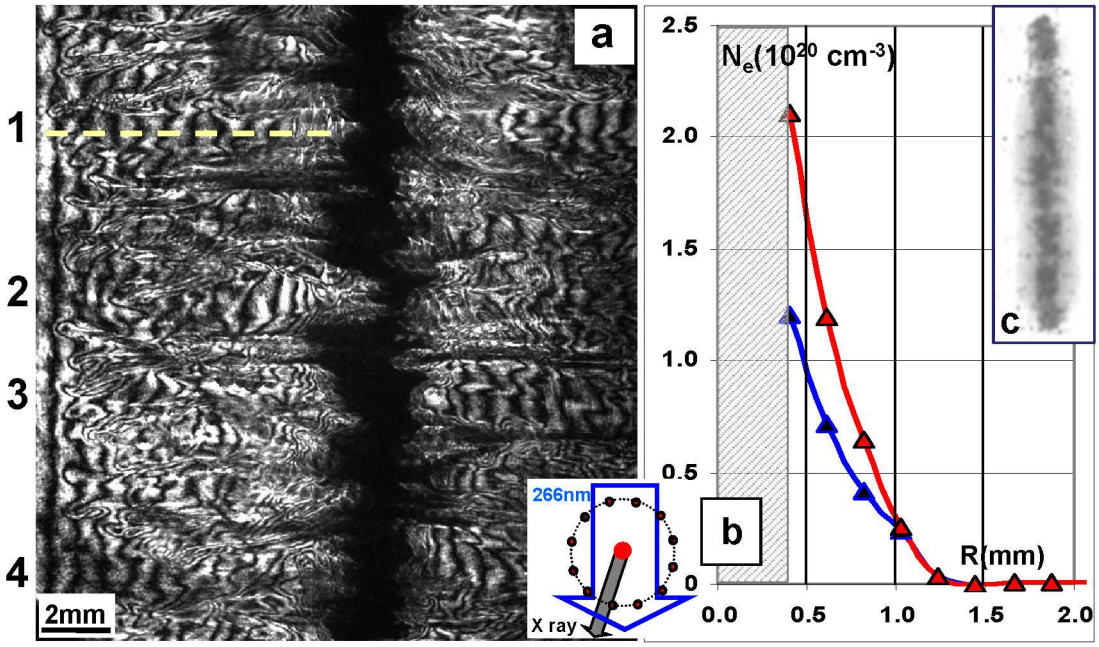

Figure 3 EU11001 01OCT2012

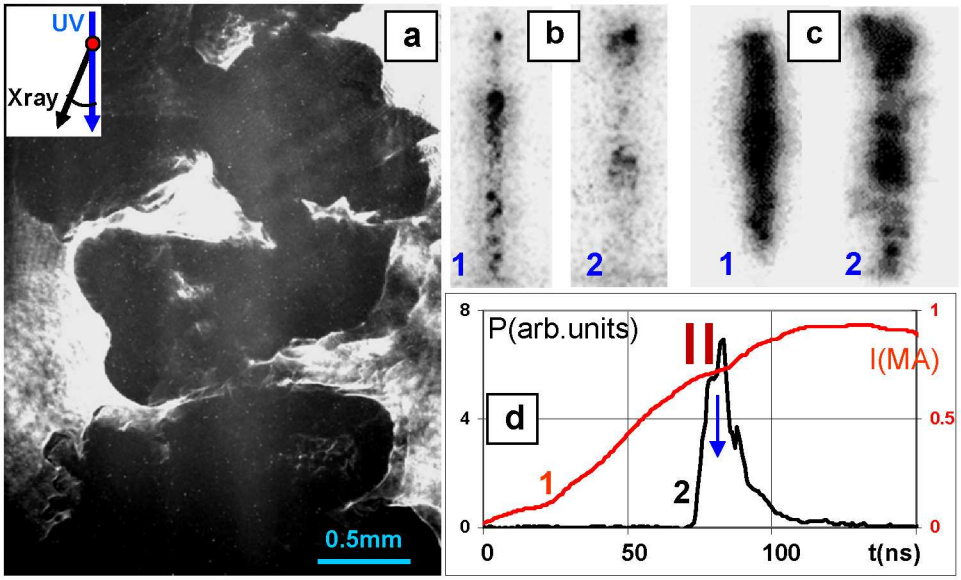

Figure 4 EU11001 01OCT2012

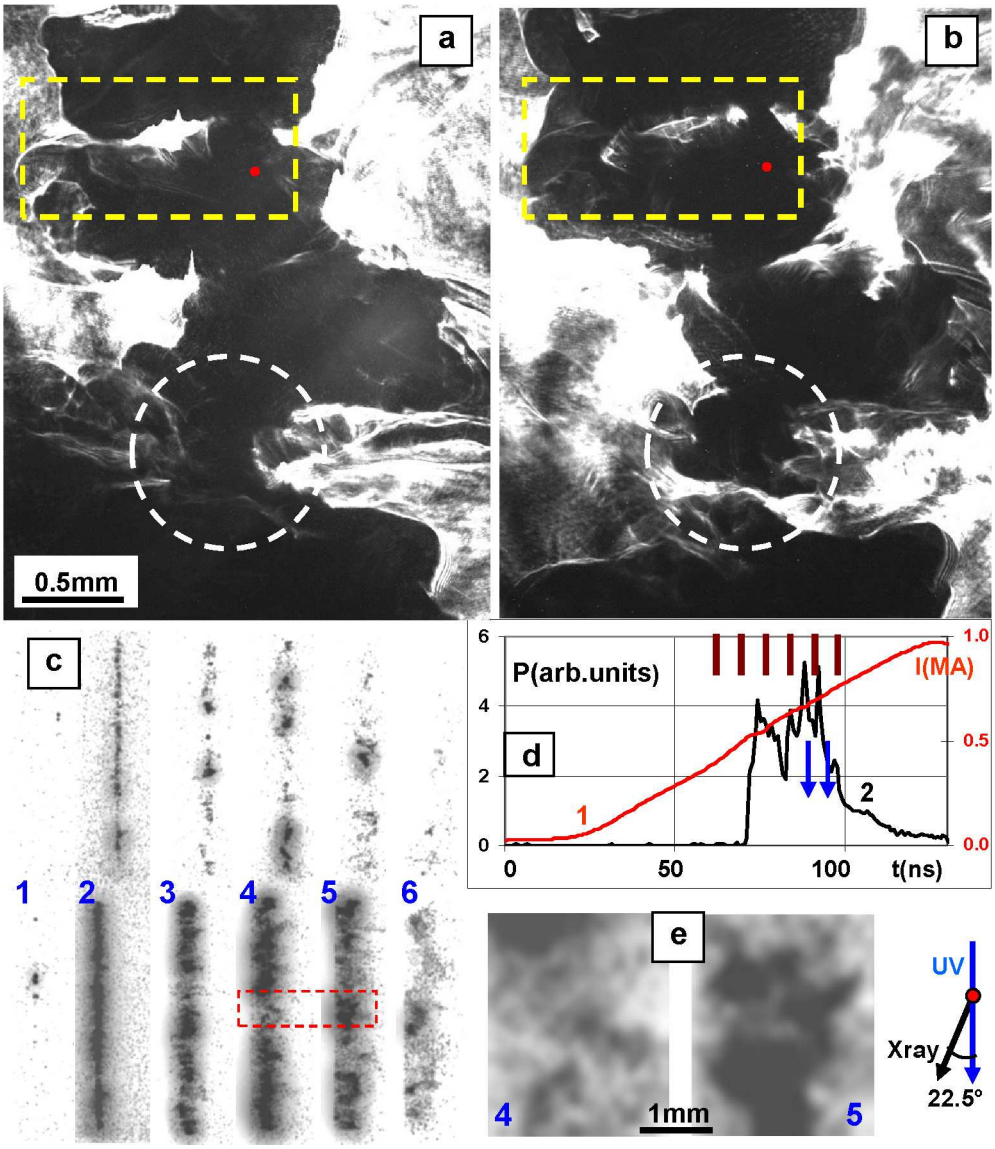

Figure 5 EU11001 01OCT2012

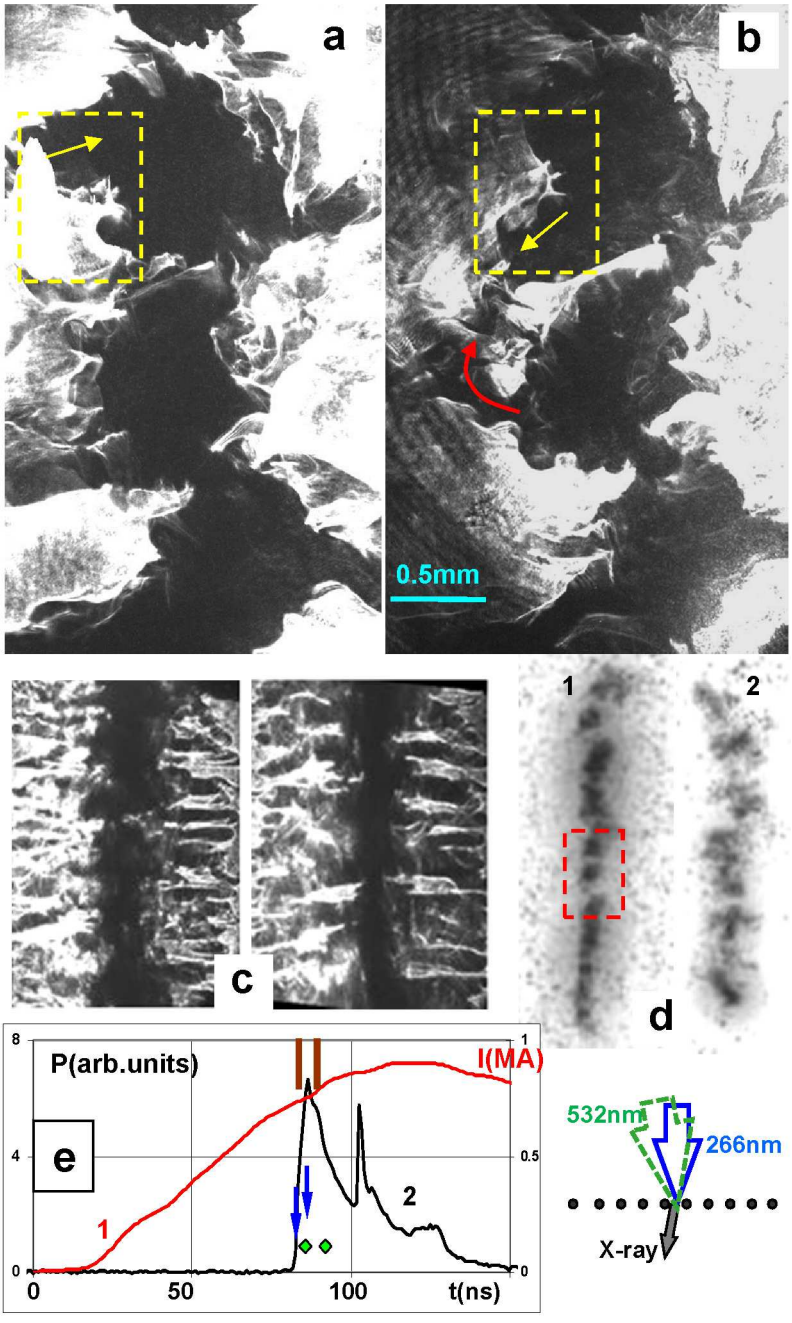

Figure 6 EU11001 01OCT2012

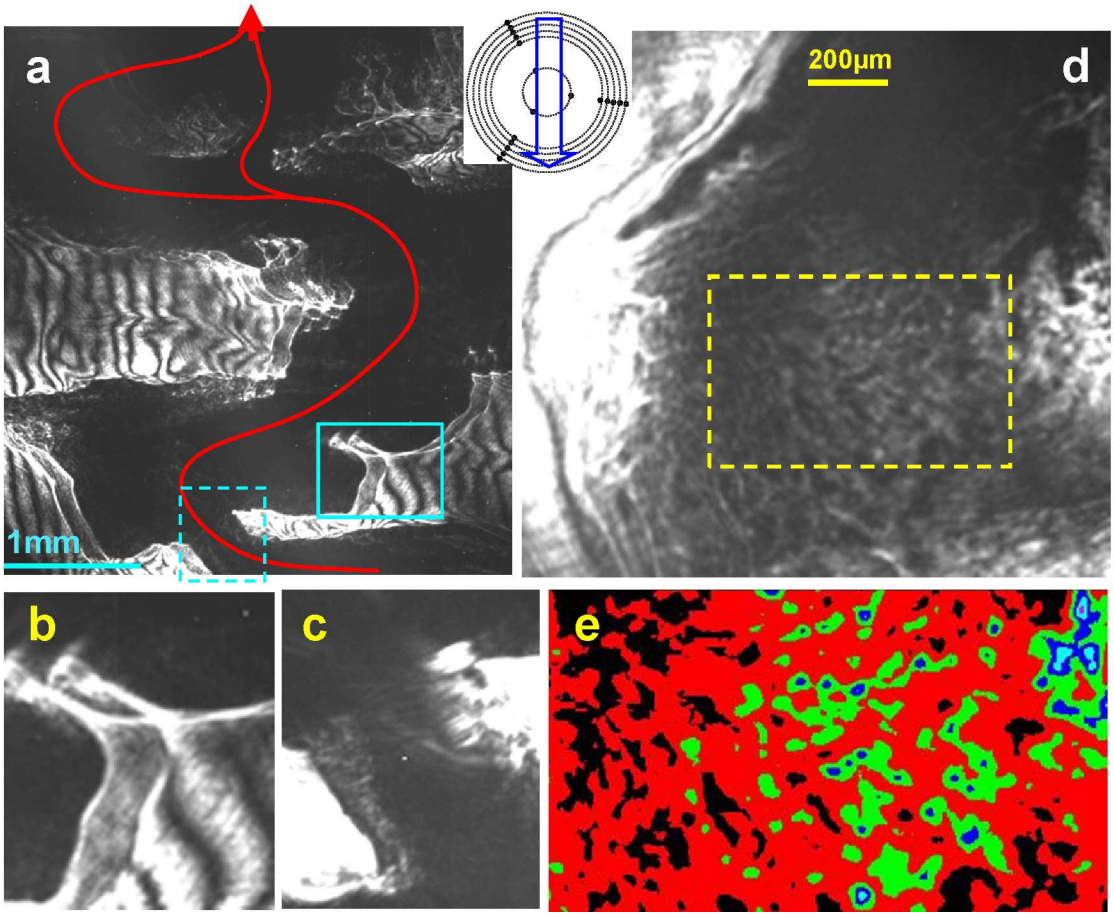

Figure 7 EU11001 01OCT2012

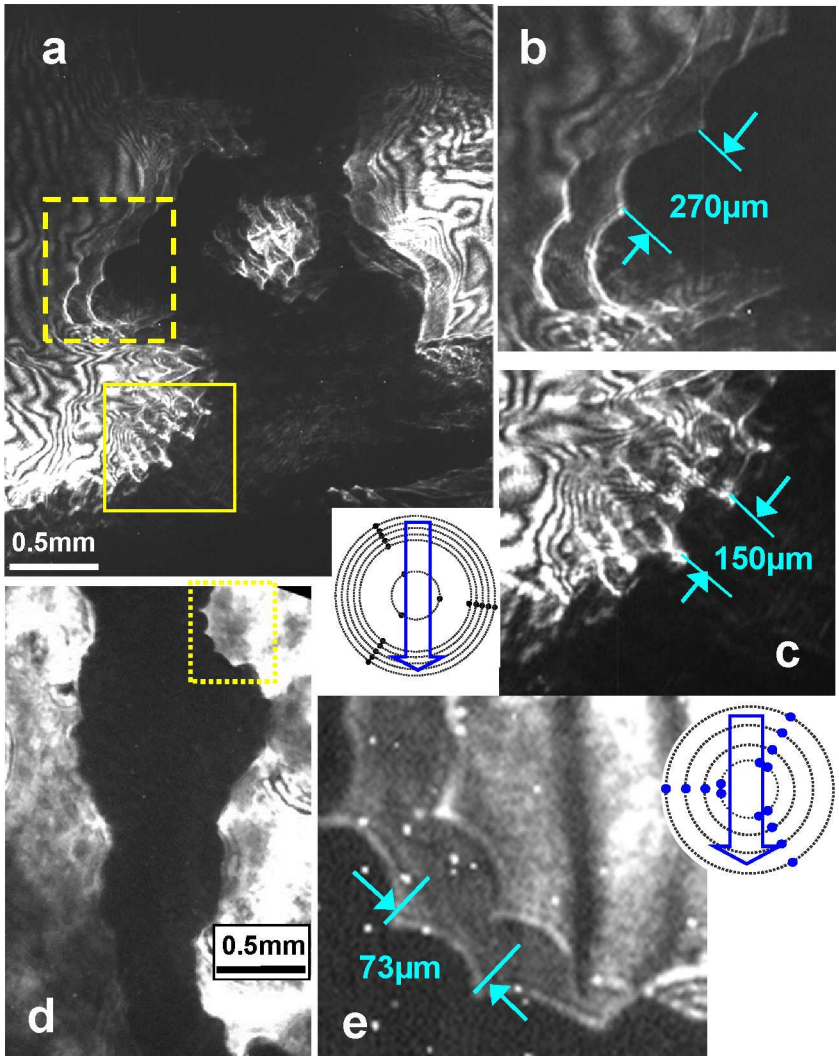

Figure 8 EU11001 01OCT2012

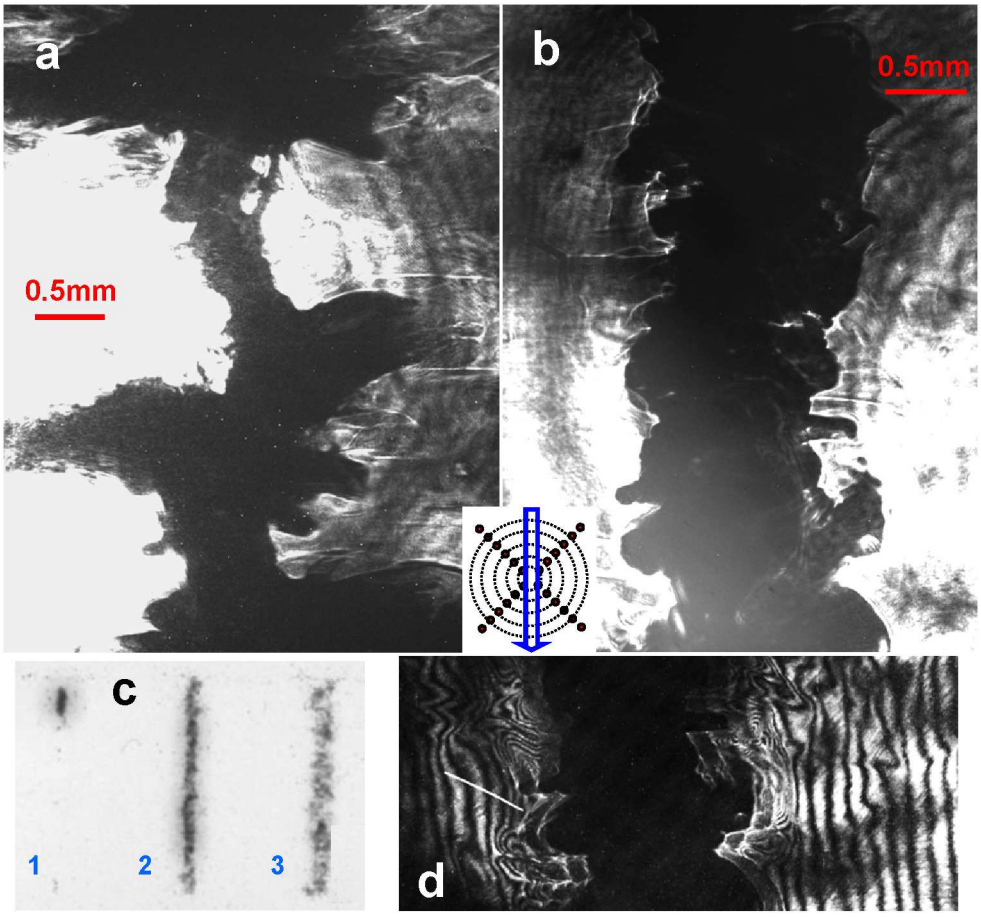

Figure 9 EU11001 01OCT2012

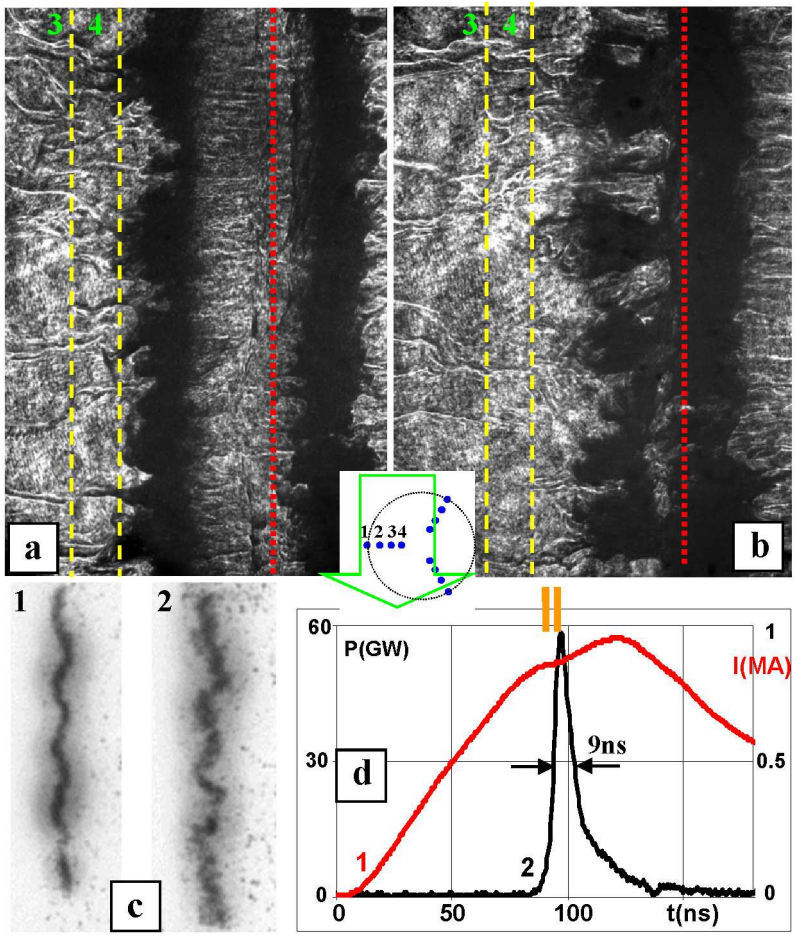

Figure 10 EU11001 01OCT2012

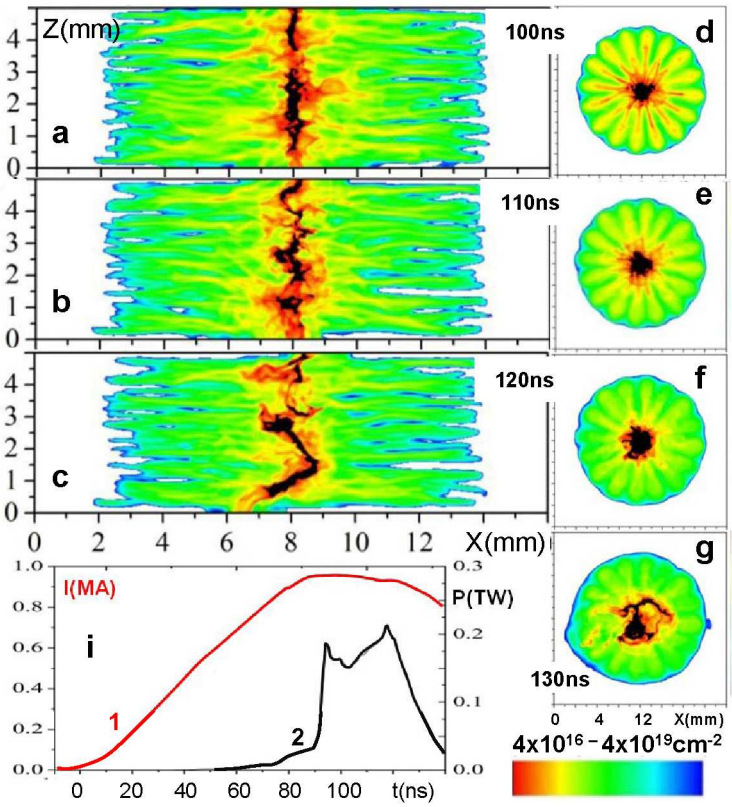

Figure 11 EU11001 01OCT2012

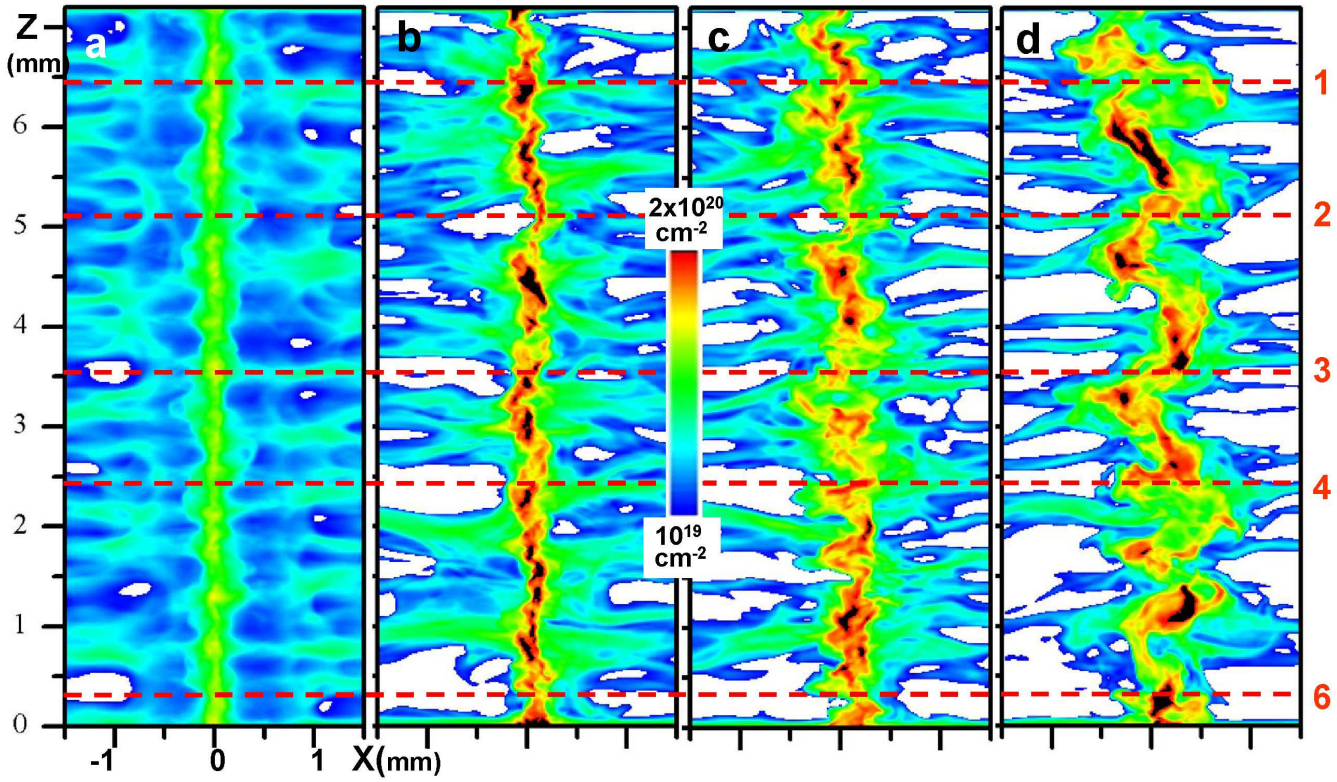

Figure 12 EU11001 01OCT2012

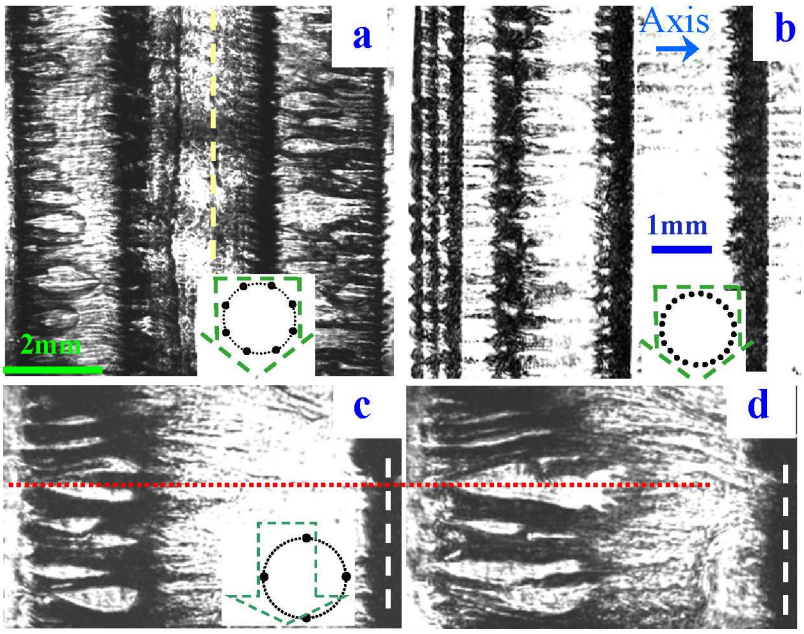

Figure 13 EU11001 01OCT2012

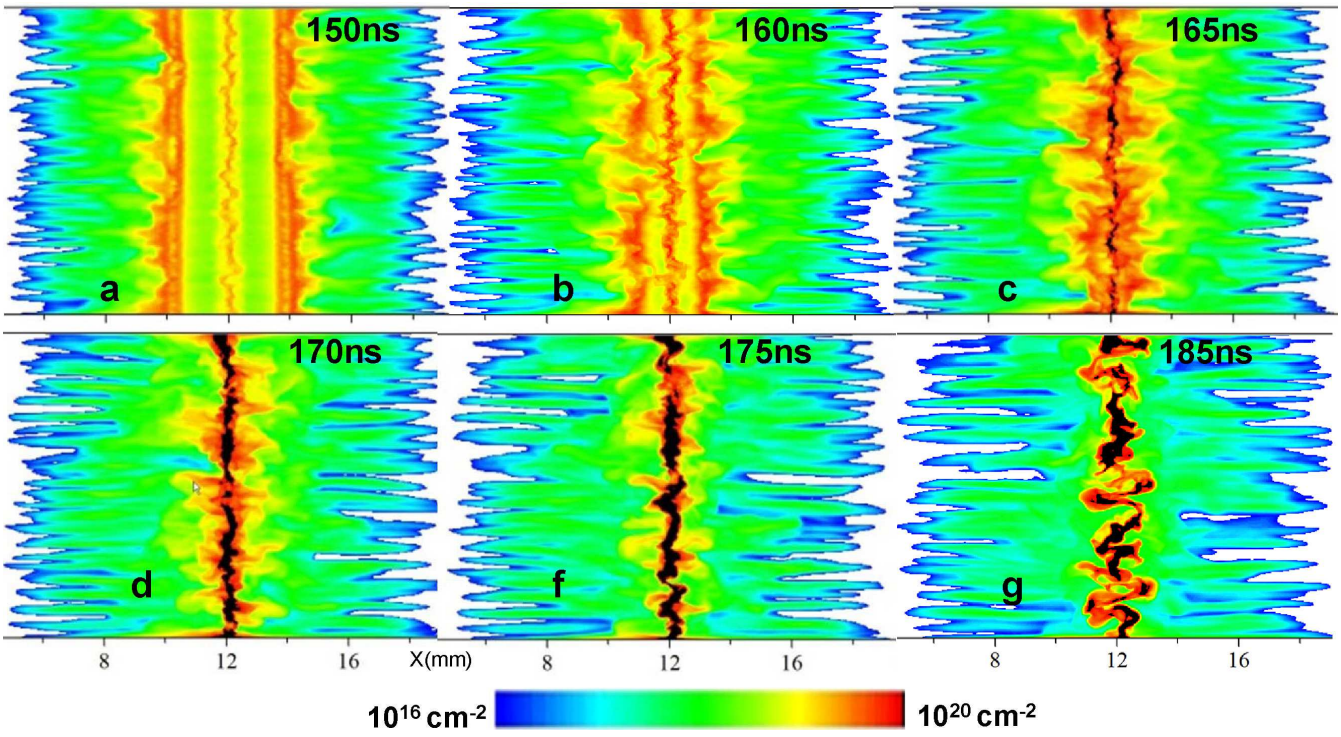

Figure 14 EU11001 01OCT2012

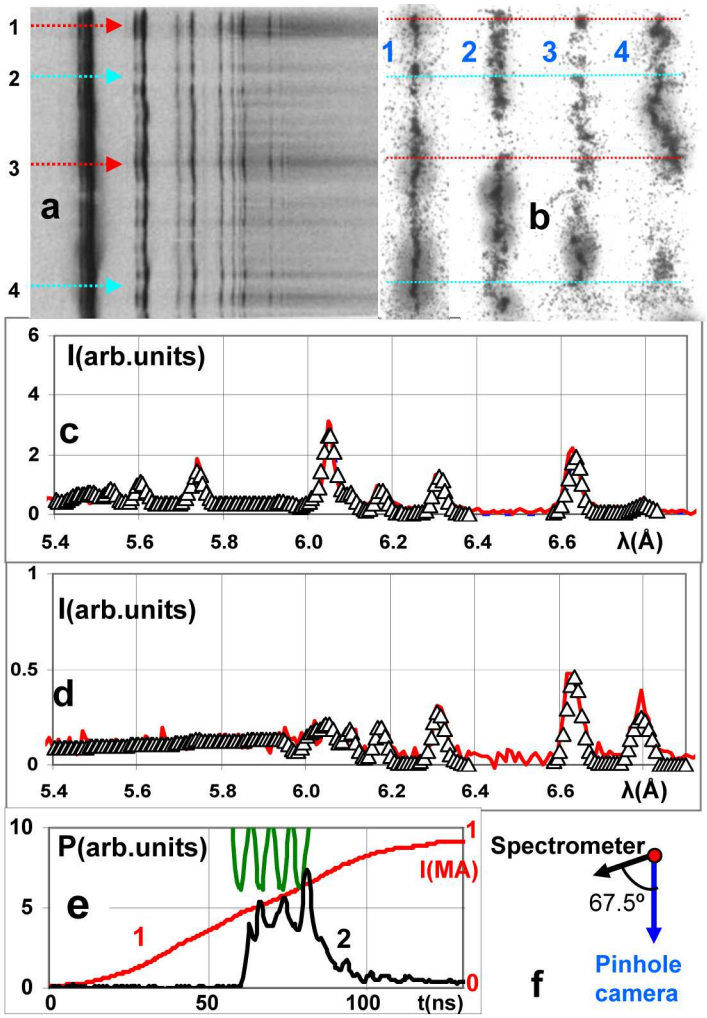

Figure 15 EU11001 01OCT2012